



# Lawrence Berkeley Laboratory

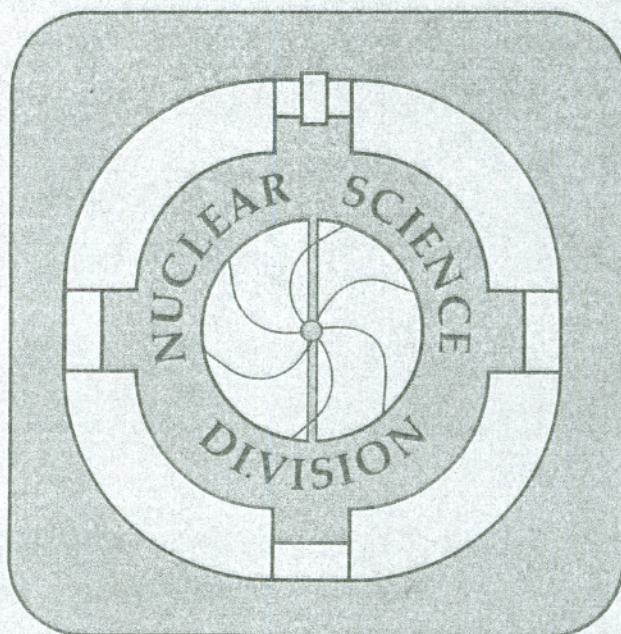
UNIVERSITY OF CALIFORNIA

Presented at the XIII Nuclear Physics Symposium,  
Oaxtepec, Mexico, January 3–7, 1990, and  
to be published in the Proceedings

## Complex Fragment Production in 50 MeV/A $^{197}\text{Au} + ^{12}\text{C}$ , $^{27}\text{Al}$ , and $^{\text{nat}}\text{Cu}$ Reactions

G.F. Peaslee, L.G. Moretto, and G.J. Wozniak

April 1990





#### DISCLAIMER

This document was prepared as an account of work sponsored by the United States Government. Neither the United States Government nor any agency thereof, nor The Regents of the University of California, nor any of their employees, makes any warranty, express or implied, or assumes any legal liability or responsibility for the accuracy, completeness, or usefulness of any information, apparatus, product, or process disclosed, or represents that its use would not infringe privately owned rights. Reference herein to any specific commercial products process, or service by its trade name, trademark, manufacturer, or otherwise, does not necessarily constitute or imply its endorsement, recommendation, or favoring by the United States Government or any agency thereof, or The Regents of the University of California. The views and opinions of authors expressed herein do not necessarily state or reflect those of the United States Government or any agency thereof or The Regents of the University of California and shall not be used for advertising or product endorsement purposes.

Lawrence Berkeley Laboratory is an equal opportunity employer.



LBL - 29014

**Complex Fragment Production in 50 MeV/A  
 $^{197}\text{Au} + ^{12}\text{C}$ ,  $^{27}\text{Al}$ , and  $\text{natCu}$  Reactions**

G.F. Peaslee, L.G. Moretto and G.J. Wozniak

Nuclear Science Division, Lawrence Berkeley Laboratory  
1 Cyclotron Road, Berkeley, CA 94720

April 1990

This work was supported by the Director, Office of Energy Research, Division of Nuclear Physics of the Office of High Energy and Nuclear Physics of the U.S. Department of Energy under Contract DE-AC03-76SF00098





# Complex Fragment Production in 50 MeV/A $^{197}\text{Au} + ^{12}\text{C}$ , $^{27}\text{Al}$ , and $^{\text{nat}}\text{Cu}$ Reactions \*

G. F. Peaslee, L. G. Moretto and G. J. Wozniak  
*Nuclear Science Division,  
Lawrence Berkeley Laboratory,  
Berkeley, CA 94720 U.S.A.*

\* Presented at the XIII Nuclear Physics Symposium,  
Oaxtepec, Mexico, January 3-7, 1990

## Abstract

Complex fragment ( $Z > 6$ ) production was studied in three reverse-kinematic reactions: 50 MeV/A  $^{197}\text{Au} + ^{12}\text{C}$ ,  $^{27}\text{Al}$ , and  $^{\text{nat}}\text{Cu}$ . Typical inclusive cross sections are shown, as well as exclusive results for 2-, 3-, and higher-fold events. Reconstructing the source velocity of these fragments and using a simple incomplete fusion model gives a reliable measure of the impact parameter and excitation energy of the reactions producing these fragments. A clear progression from peripheral (cold) events to more central (very hot) events is seen as a function of source velocity. The primary production of fragments in the  $^{197}\text{Au} + ^{12}\text{C}$  and  $^{27}\text{Al}$  reactions is consistent with statistical emission from a thermalized source, up to approximately 5 MeV/A of excitation energy. For the  $^{\text{nat}}\text{Cu}$  target, another significant source of fragment emission is observed.

## 1 INTRODUCTION

Heavy ion accelerators allow us to study nuclear systems under extreme conditions of excitation energy and angular momentum. For an increase in the mass of the accelerated nucleus, the range of possible impact parameters for the collision increases, and the resultant energy and angular momentum ranges increase as well. By systematically studying a series of heavy projectile and target combinations, and unfolding the impact parameter of the collision experimentally, it is possible to study nuclear matter from a very cold state (peripheral reactions) to a very hot state (central reactions).

In this work, we present the results of an experimental study utilizing an accelerated beam of  $^{197}\text{Au}$ , incident on three lighter targets. At 50 MeV/A these reactions produce heavy nuclei at the limit of stability, and tend to have copious complex fragment ( $Z > 6$ ) production[1]. We have measured this complex fragment production, using the technique of "reverse kinematics" to increase our detection efficiency. These data provide fresh insight on the open questions concerning the limits of linear and angular momentum transfer, as well as a better determination of the reaction mechanisms involved.

There have been a number of recent studies[2-8] concerning the reaction mechanisms that lead to multifragmentation, and whether the multifragment production process is



sequential or prompt in nature. We can demonstrate that a simple picture of incomplete momentum transfer and the subsequent thermalization and statistical decay of a hot source accounts for most of the complex fragment production at lower excitation energies. Indeed, this simple reaction mechanism continues to dominate up to excitation energies of approximately 5 MeV/A. For these heavy  $^{197}\text{Au}$  nuclei, this translates to around 1 GeV of total excitation! At higher excitation energies, which are achieved with the central reactions of  $^{nat}\text{Cu}$  target, other multifragment production mechanisms begin to dominate.

## 2 THE EXPERIMENT

This experiment was performed at the LBL Bevalac, and was designed to complement several systematic studies that have utilized lighter Nb and La beams[4, 9, 10, 11]. To concentrate on the multifragmentation processes that occur around 50 MeV/A, a heavy system was used to facilitate the detection of the many reaction products. The heavier the initial system is, the heavier the resultant reaction products will be. For example, even though there may be four or five fragments resulting from a single collision, with a gold projectile each of these fragments will still be large enough to distinguish it from charged particle evaporation, which abounds at these energies.

We have used the technique of "reverse kinematics" to study these reactions. This means the heavy gold nucleus is accelerated, and impinges on the lighter targets, as shown schematically in Fig. 1. This technique solves two important technical problems which plague conventional heavy ion experiments: the energy and angular acceptance of the detectors. By having the heavy projectile strike light targets, the reaction products are all focused forward into a cone about the beam. Rather than constructing an expensive  $4\pi$  detector, a smaller detector can be built at forward angles, that will still be able to cover all the possible fragment emission angles. A generic detector of this type is shown as the solid line in Fig. 1. All fragments emitted into the cross-hatched area of the figure will be detected. Similarly, due to the large center-of-mass velocity ( $V_{cm}$ ), most of the reaction products will have energies near that of the projectile, even if their Coulomb repulsion energies are small. Low energy fragments, or fragments which are emitted backwards in the center-of-mass and are difficult to detect in normal kinematics are very energetic in "reverse kinematics". With sufficient beam velocity, it can be seen in Fig. 1 that there will be no serious detector threshold effects in "reverse kinematics".

Of course, this technique is not free of disadvantages. All of the reaction products are compressed into a small area of real space, and any detection system needs to have excellent energy and angular resolution to differentiate the products. Also, the detection system needs to have sufficient granularity to minimize multi-hit problems, especially when studying multifragment events. To overcome these difficulties, we have designed and constructed a Si-Si-Plastic telescope array[12, 13]. An expanded view of one of these telescopes is shown in Fig. 2. In front there is a 300 micron thick position-sensitive Si detector that measures approximately  $20\text{ cm}^2$ . This is an np-diffused junction diode that uses resistive division along one surface to obtain position resolution of 3 mm in the X-plane. Behind it is stacked a 5 mm thick position-sensitive lithium-drifted silicon device, with 3 mm position resolution in the Y-plane. A second 5 mm Si device can be stacked behind this one for additional stopping power. All of these Si detectors are mounted in front of a 7.5 cm plastic scintillator and attached photomultiplier tube. Signals are passed



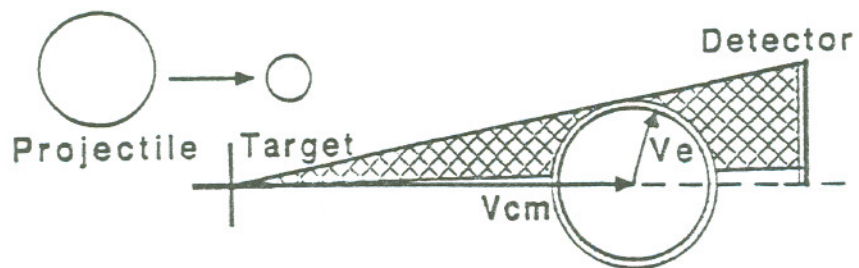


Figure 1

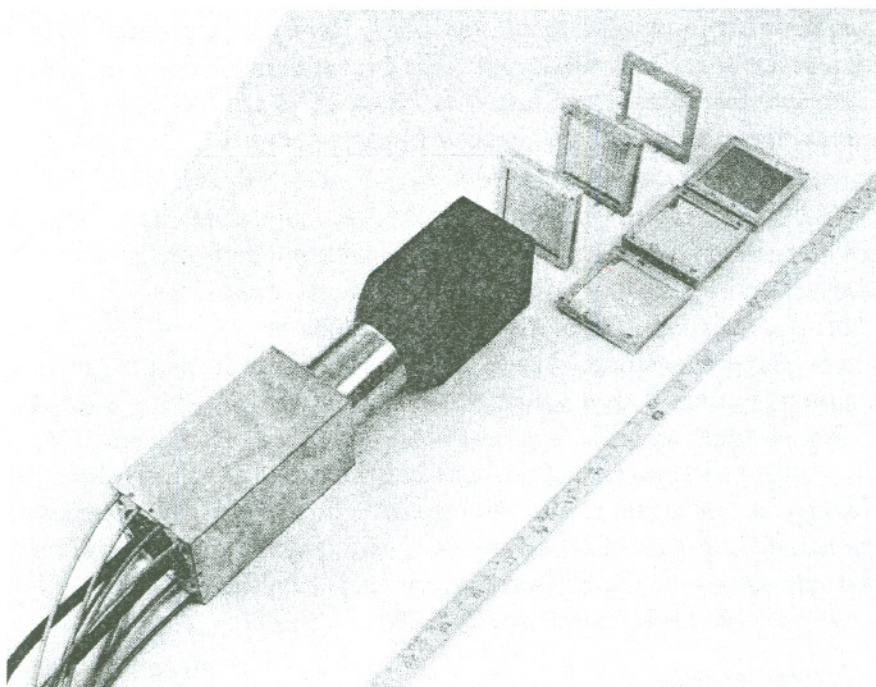


Figure 2

CBB 889-9134

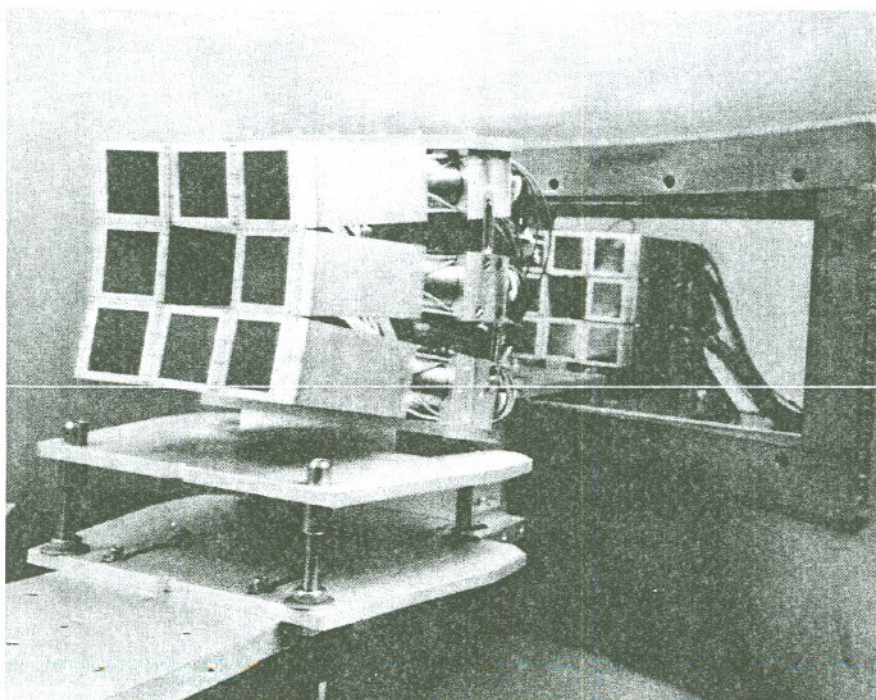


Figure 3

CBB 889-9132



through the frames of each device, which are kept as small as possible for close-packing of the array.

In Fig. 3 the specific experimental set-up for the gold beams is shown. Two concentric rings of 8 telescopes were centered about the beam, one located approximately 37 cm from the target, and the second located approximately 103 cm from the target. This geometry has the advantage of greater granularity closest to the beam, and maximum angular coverage for the fewest telescopes. The downstream ring was as close as  $1.8^\circ$  to the beam, and the upstream ring reached as far as  $16^\circ$  from the beam. The detection system subtends approximately 64% of the solid angle between  $1.8^\circ$  and  $16^\circ$ .

The solid-state Si detectors allow for very precise energy measurements, usually within 0.5% of the total energy deposited. Pulse height defect corrections have been made with data from lower energies[14] and preliminary studies made between 10 and 100 MeV/A at the Bevalac[15]. With this type of accuracy, individual charge identification is possible up to  $Z \approx 50$ . An example of typical charge resolution is given in Fig. 4 (left frame) for a lanthanum-induced reaction. The Si devices are self-calibrating in position, in that there are conductive strips 3 mm apart, which can be seen clearly in a typical position spectrum in Fig. 4 (right frame). This position information yields angular resolution to better than  $0.5^\circ$ . The combination of this excellent position and energy resolution, as well as the granularity of the array, allows the reconstruction of the multifragment events in "reverse kinematics". In the following analysis, only fragments that were heavy enough to be stopped completely in the Si detectors are included. This constrains the minimum charge detected to be between  $Z = 6$  and  $Z = 10$ .

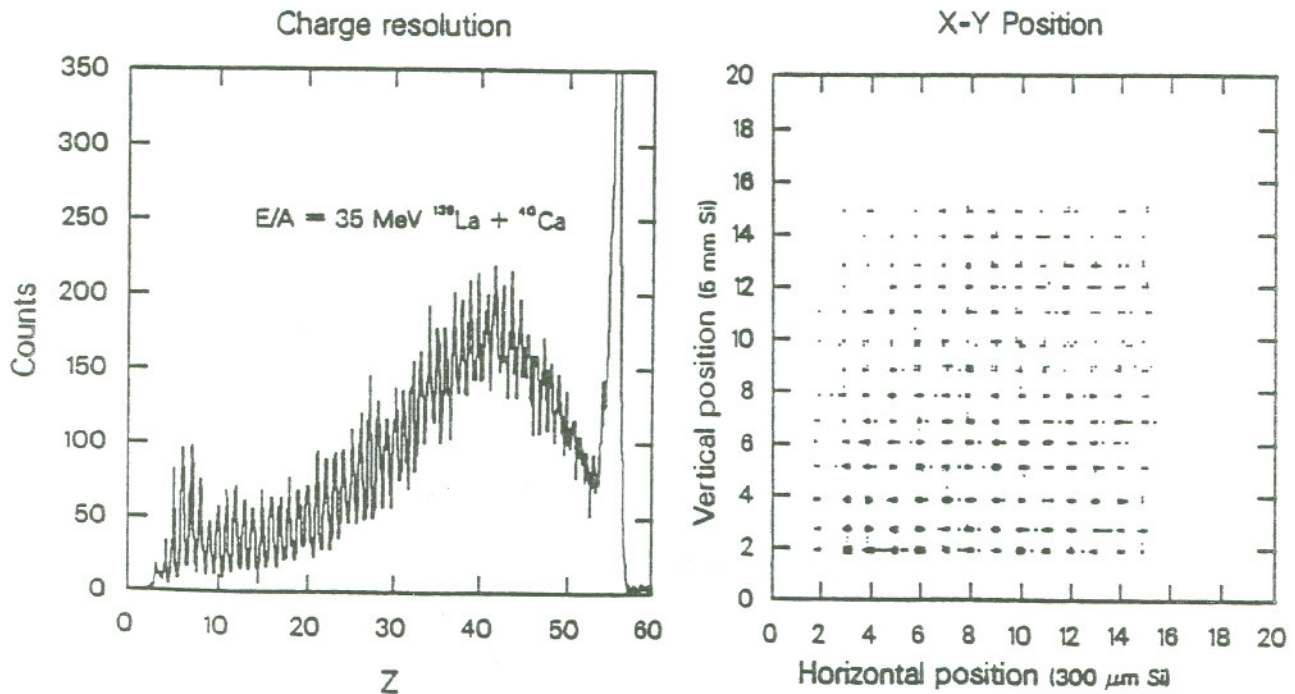


Figure 4



### 3 RESULTS

#### 3.1 Singles

At a bombarding energy of 50 MeV/A, we are well into the incomplete fusion reaction regime. Complete fusion of the target and projectile is no longer feasible energetically, and typically these nuclear reactions are described as incomplete fusion reactions where mass is transferred from the lighter nucleus to the heavier. In "reverse kinematics" this means that part of the target is lost, through preequilibrium particle emission or from simple cleavage of the target nucleus. A fraction of the target mass is transferred to the projectile, depending on the impact parameter in the entrance channel. Obviously, for a given target and projectile combination, an average mass (and hence momentum) transfer can be used to describe the incomplete fusion mechanism at any specific bombarding energy. Systematic studies of this linear momentum transfer have been made at lower energies[16, 17]. In Table 1, these systematics have been extended to include the 50 MeV/A  $^{197}\text{Au} + ^{12}\text{C}$ ,  $^{27}\text{Al}$ , and  $^{nat}\text{Cu}$  reactions studied here. The corresponding average excitation energy of the composite system created in each reactions is also listed. It is obvious that large amounts of excitation energy are available in these reactions. This large excitation energy can be expected to dissipate via many different exit channels, and reconstruction of an average event could be quite difficult.

Table 1:

Reaction	% LMT	$A_{CN}$ (amu)	$E_{CN}^*$ (MeV)
50 MeV/A $^{197}\text{Au} + ^{12}\text{C}$	0.57	204	333
50 MeV/A $^{197}\text{Au} + ^{27}\text{Al}$	0.56	212	698
50 MeV/A $^{197}\text{Au} + ^{nat}\text{Cu}$	0.52	230	1411

To get a quick overview of the reactions, singles data can be quite informative. An obvious start is the velocity spectra of a particular reaction product in terms of  $V_{\parallel}$  versus  $V_{\perp}$ . Figure 1 depicted a schematic diagram of a binary decay in velocity space, with a large velocity of the composite system ( $V_{cm}$ ), and a relatively small emission velocity ( $V_e$ ) for a fragment emitted from the composite system. For any specific fragment, there will be a Gaussian distribution in  $V_e$ , centered around a mean value that is mostly determined from Coulomb repulsion. A projection of this sphere of emission onto  $V_{\parallel}$  versus  $V_{\perp}$  will lead to a "Coulomb ring" of cross section, characteristic of the particular charge of the detected fragment, and the total Coulomb energy of the system. A series of these "Coulomb rings" are shown in Fig. 5 for the 50 MeV/A  $^{197}\text{Au} + ^{12}\text{C}$  reaction. Note that as the detected fragment charge increases, the average  $V_e$  decreases, and the rings shrink. In a binary decay, the lighter emitted fragments have the higher velocities, from simple momentum conservation. Significant multifragmentation decay leads to a filling-in of the ring. In Fig. 6, a comparison of  $Z=20$  fragments from 50 MeV/A  $^{197}\text{Au} + ^{12}\text{C}$ ,  $^{27}\text{Al}$ , and  $^{nat}\text{Cu}$  reactions is shown. A strong binary component is observed in each case, as indeed the binary fission of gold dominates the singles cross sections. However, there is an obvious filling-in of the 'Coulomb ring' for the  $^{nat}\text{Cu}$  target, relative to the other two. This could



50 MeV/A  $^{197}\text{Au} + ^{12}\text{C}$

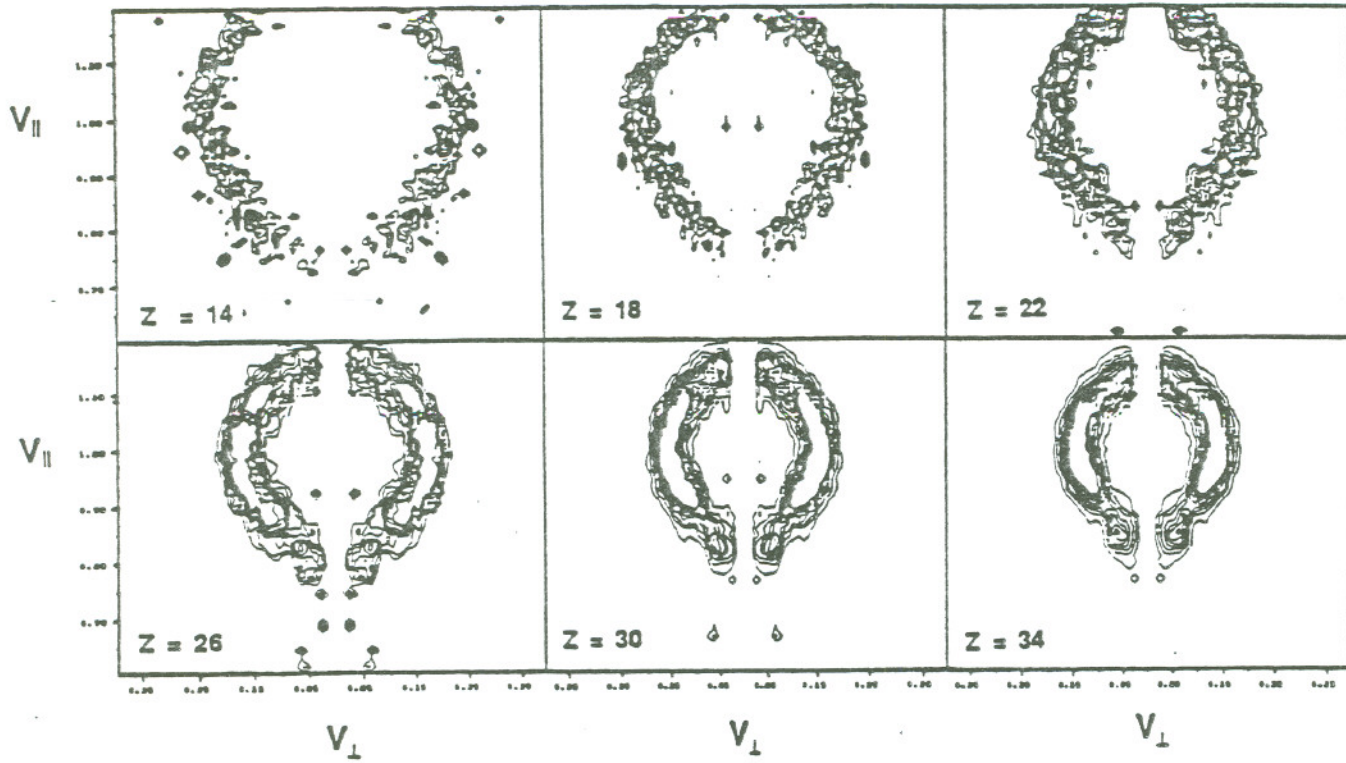


Figure 5

50 MeV/A  $^{197}\text{Au} + ^{12}\text{C}, ^{27}\text{Al}, \text{natCu}$

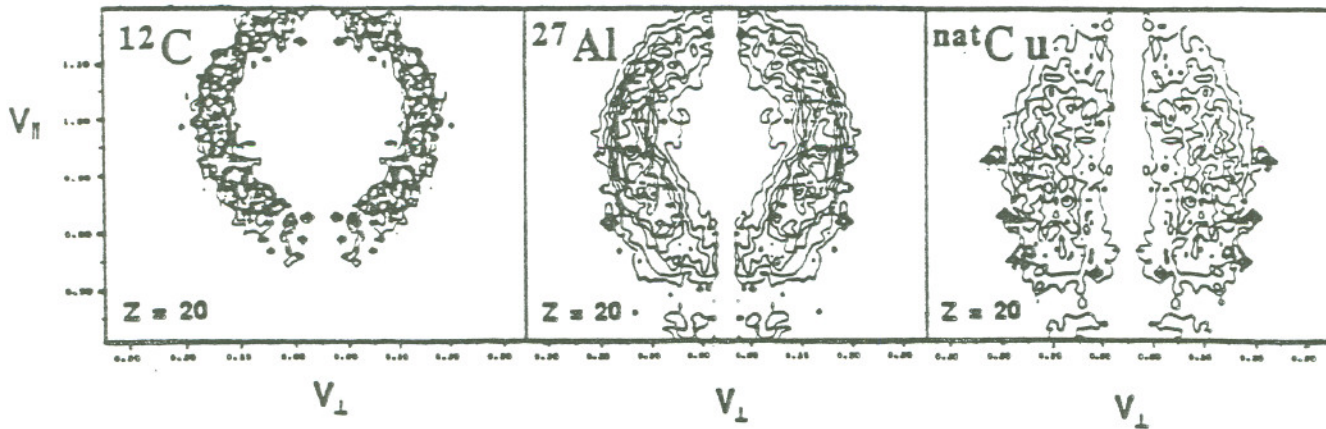


Figure 6



be due to two different reasons:  $Z=20$  fragments could be produced in abundance from other decay mechanisms for the  $^{nat}\text{Cu}$  target (such as sequential multifragmentation), or the larger target could provide a broader range of impact parameters, and hence a broad range of momentum transfers, which effectively smears out the  $V_{cm}$  distribution. Note that the size of the circles increases slightly with the more massive targets, indicating a larger source for these fragments.

From the "Coulomb rings", it is trivial to extract singles angular distributions in terms of  $\frac{d\sigma}{d\Omega}$ , and to integrate the isotropic component to give the integrated singles cross sections as a function of charge ( $\sigma_Z$ ). These integrated cross sections are given in Fig. 7 for each of the three targets. The singles yields are dominated by the symmetric fission of a gold-like projectile. This is because even a single nucleon transfer will impart enough energy to the gold projectile to allow fission, and these peripheral reactions dominate the singles cross sections. There are literally barns of cross section available for these processes. It is interesting to note, however, that the  $^{nat}\text{Cu}$  target has a significant yield of lighter fragments, comparable to the cold fission yields. In the angular distributions (not shown) it can be seen that these light fragments are strongly forward-peaked, but even the isotropic component of this cross section increases strongly for lighter fragments. This is a clear indication of a reaction process that is available to the nuclear systems formed with the  $^{nat}\text{Cu}$  target, that appears not to dominate for the lighter targets. This is most probably related directly to the amount of excitation energy available to the reacting system, which is greatest for the  $^{nat}\text{Cu}$  target.

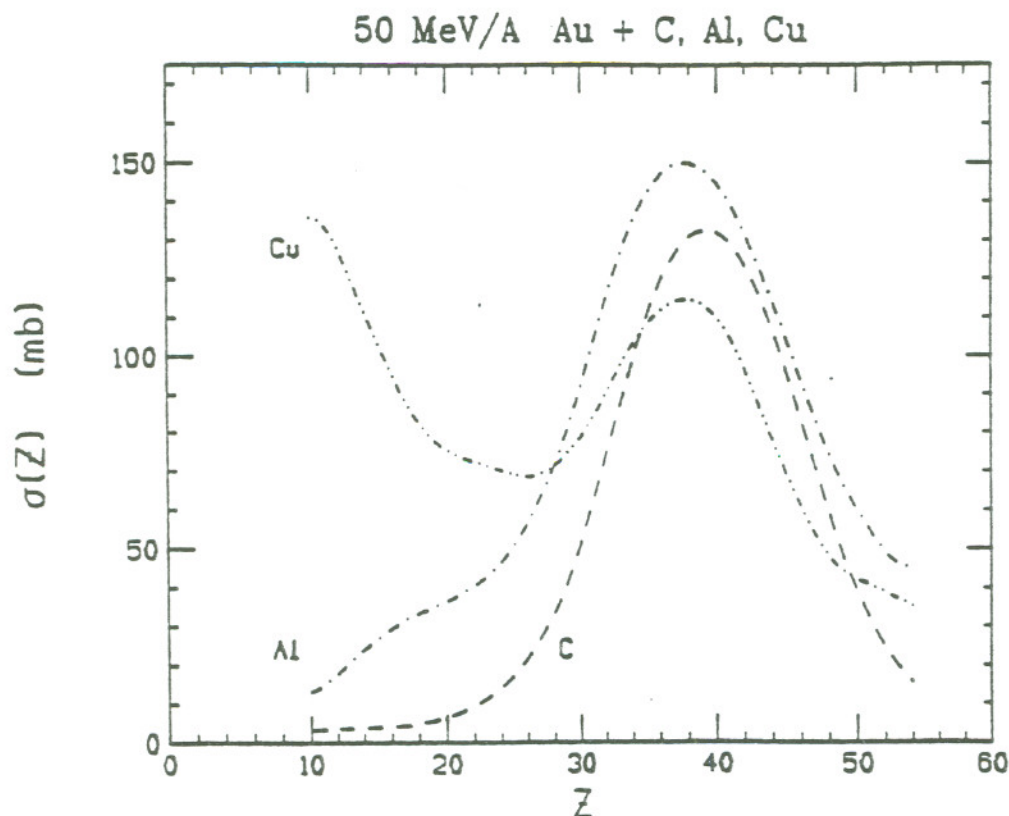


Figure 7



### 3.2 Multiplicity Requirements

To further untangle the competing decay processes, the next logical step is to look at the coincidence events. An  $n$ -fold event is defined here as an event where  $n$  events are detected; there will, of course, be higher order events mixed in with these events, when one or more fragments have escaped detection. Figure 8 gives an overview of the reaction products from the three targets, for 2-fold and 3-fold coincidence events. For the 2-fold coincidences (the left column), the detected fragment charge of one fragment is plotted against the fragment charge of the second. The predominant feature of all three plots is a well defined ridge running diagonally along a line that can be approximated by:  $Z_1 + Z_2 = 79$  (dashed line). This ridge is strongly peaked towards symmetry, and corresponds to the peripheral reactions that lead to fission of the gold projectile. There is also a marked filling-in of the light fragment - light fragment coincidences as the target charge increases. For the  $^{nat}\text{Cu}$  target, the light fragment coincidences are comparable in cross section to the peripheral reactions, as was noted in the singles results.

For the 3-fold events (the right column of Fig. 8), the fragment charge of one fragment is plotted against the sum of the charges of the other two fragments. The ordering of the fragments is chosen randomly within each event. Several interesting changes can be observed, most noticeable of which is the absence of the peripheral events. As would be expected, the very peripheral reactions can lead to fission of the gold projectile, but they cannot produce three-body decays. Secondly, although the peripheral reactions have been gated out, there is still a distinct ridgeline of events for the  $^{12}\text{C}$  and  $^{27}\text{Al}$  targets. Notice, however, that this locus is much broader than cold fission of the projectile, and exhibits a triple-bumped shape, reminiscent of the trimodal potential barriers expected for complex fragment decay of a heavy system (see [3]). Note also, that the locus of the ridge line has shifted slightly downward, especially for the  $^{27}\text{Al}$  target, no longer centered around  $Z=79$ . This is again an indication that more central collisions are involved, because at a bombarding energy of 50 MeV/A for every extra nucleon the projectile picks up, it gains enough excitation energy to evaporate roughly two nucleons off the reaction products. Since evaporated light particles are not detected, the detected mass of the fragments will go down.

The  $^{nat}\text{Cu}$  target appears to continue this trend at first glance, however, it is impossible to say whether there is actually a ridgeline formed at all. The requirement that three fragments with  $Z \geq 6$  be detected makes an artificial hole in the spectrum below the line  $Z_1 + Z_2 + Z_3 = 18$ . The presence of a ridgeline for the lighter targets suggests that a major source of 3-fold events lies in the sequential binary decay of a composite system. This is not so obvious for the  $^{nat}\text{Cu}$  target.

### 3.3 Source Velocity Requirements

Using the excellent energy and position resolution of the detector system, another technique to analyze the data becomes possible. By vectorially summing the momentum of each fragment in a coincidence event, and dividing by the sum of the masses, it is possible to construct the source velocity of each event. This is merely:

$$\frac{\sum_i m_i v_i}{\sum_i m_i} \quad (1)$$



50 MeV/A  $^{197}\text{Au} + ^{12}\text{C}, ^{27}\text{Al}, \text{natCu}$

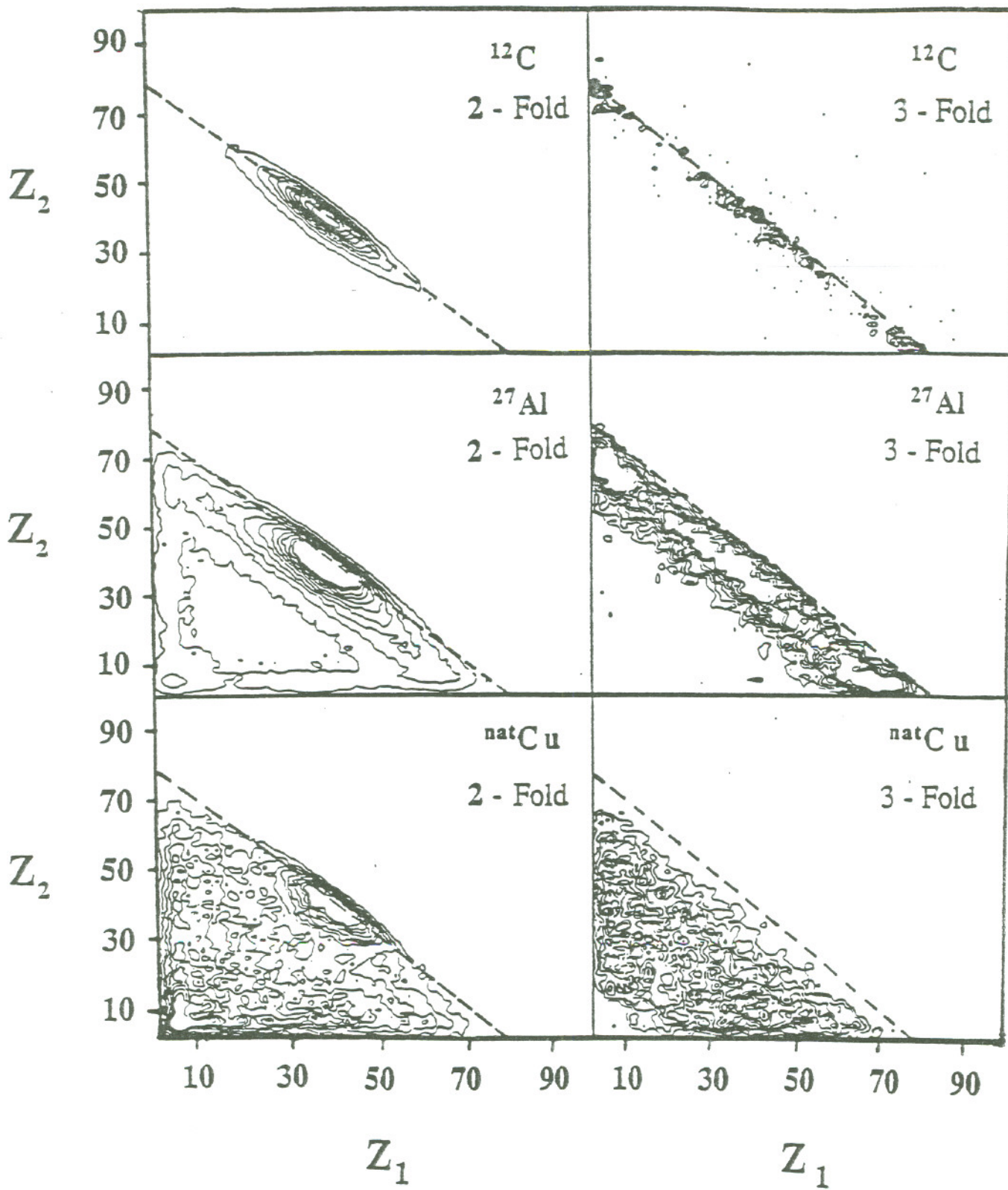


Figure 8

Given sufficient resolution, this event-by-event center of mass can be used to reconstruct the initial momentum of the emitting system (see, for example, [18]). (The mass of each fragment is calculated from the detected charge, using the mass parametrization of [9].) Once the average momentum transfer has been obtained from the source velocity, the excitation energy of the emitting source is inferred from a simple incomplete fusion model.

In Fig. 9, this inferred excitation energy is plotted against the total detected charge ( $Z$ ) of the 2-fold events, for all three targets. In this figure it can be seen that there is little or no correlation between detected charge and the velocity of the emitting system for the  $^{12}\text{C}$  target. The width of the source velocity distribution is very narrow for  $^{12}\text{C}$ , and this is interpreted to mean that there is a very narrow range of impact parameters (and hence momentum transfers) available for this reaction. The mean value of the source velocity lies roughly halfway between the velocity of the projectile and the velocity of the compound nucleus formed from the complete fusion of the target and projectile. This means that roughly half of the  $^{12}\text{C}$  target gets transferred to the gold projectile on average, together with approximately 300 MeV of excitation energy. Table 2 lists the complete momentum transfer systematics measured in this experiment, as a function of the detected multiplicity of the event.

Table 2:

Event Multiplicity	% Linear Momentum Transfer		
	$^{12}\text{C}$ Target	$^{27}\text{Al}$ Target	$^{nat}\text{Cu}$ Target
2-fold	0.374	0.412	0.247
3-fold	0.500	0.560	0.313
4-fold		0.567	0.373
5-fold		0.800	0.701

For the 2-fold events from the  $^{27}\text{Al}$  and  $^{nat}\text{Cu}$  targets, there is a much broader source velocity distribution, which shows a strong correlation with detected fragment charge between  $Z = 80$  and  $Z = 65$ . The part of these spectra that shows a linear decrease in detected charge with decreasing source velocity, merely represents the region of increasing momentum transfer, hence increasing excitation energy deposited to the composite system. Since these figures are for 2-fold events, this region encompasses peripheral events as well as the more central events. There is a region of lower detected charge, above 750 MeV of excitation, that seems to be independent of the velocity of the source, which could be due to the occurrence of 3- or higher-fold events where one or more fragments escaped detection. However, using the multiplicity information and the source velocity information yields a more comprehensive picture up to 1000 MeV of excitation and beyond.

In Fig. 10, the excitation energy of the emitter is again extracted from the source velocity, and the percentage of  $n$ -fold events (as a fraction of the total  $n$ -fold events) is plotted against it. Singles are not shown on this figure, since our efficiency for detecting evaporation residues is likely to be significantly different (and lower) than our coincidence efficiency. It is remarkable that all targets show a smooth increase in multiplicity of the higher-fold events, even up to 5 MeV/A of excitation and beyond. This is very similar to statistical decay calculations of sequential multifragmentation, which also show a smooth



50 MeV/A  $^{197}\text{Au} + ^{12}\text{C}$ ,  $^{27}\text{Al}$ ,  $^{\text{nat}}\text{Cu}$  (2-body)

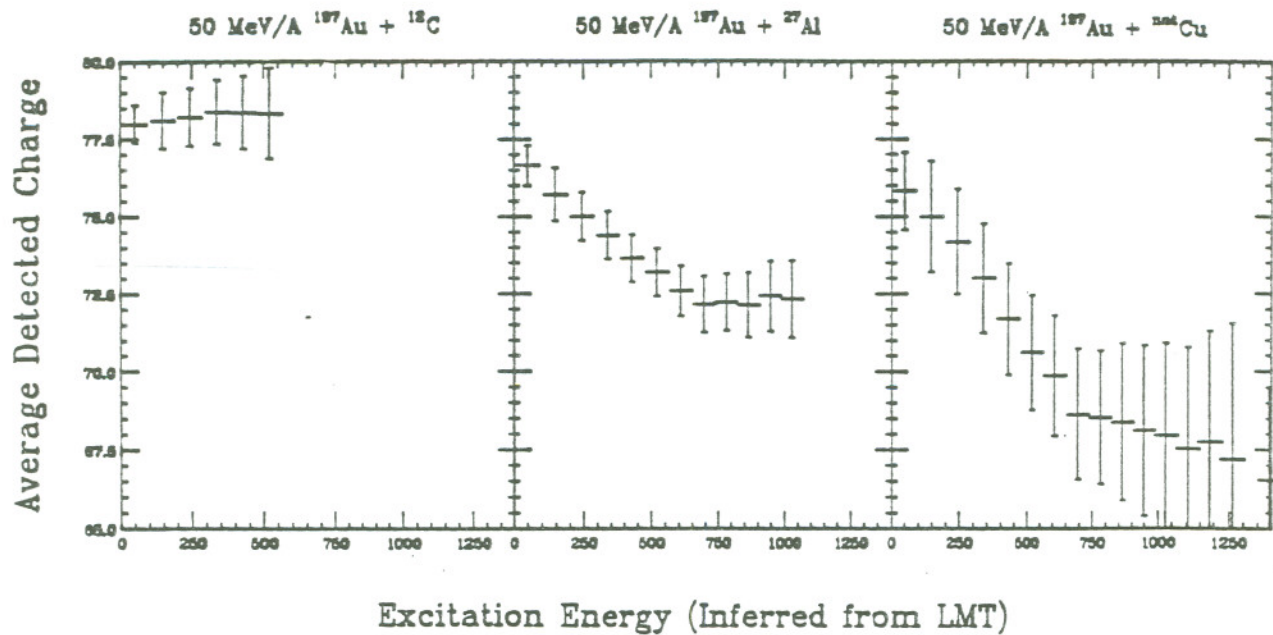


Figure 9

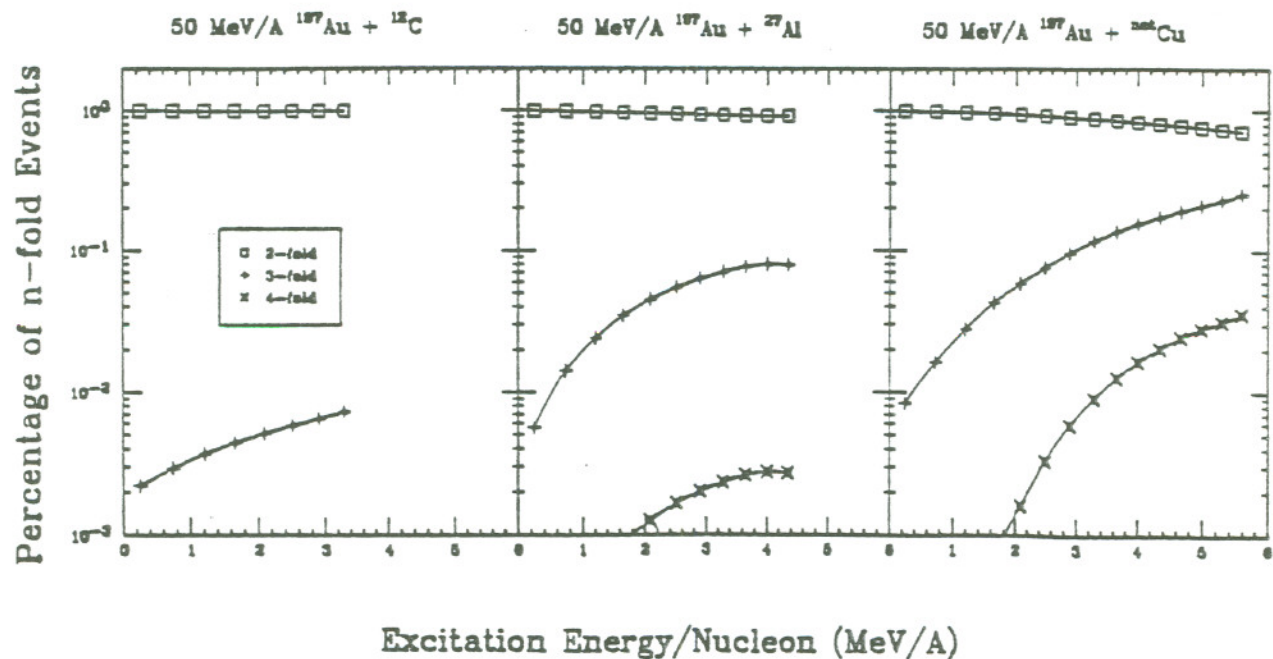


Figure 10

increase in multiplicity as a function of excitation energy [19]. This trend was also seen, independent of target, for La systematics at 35 and 40 MeV/A [20]. This trend confirms that the source velocity can be a very useful tool for extracting an excitation function with only one bombarding energy, by using the impact parameter of the collision instead. It also establishes the source velocity as a gating condition to examine the decay mechanism of hot and heavy nuclear systems at different excitation energies. This tool is used extensively in the following sections.

### 3.4 $Z_1 - Z_2$ Gated by $V_{source}$

As an example of the power of the source velocity gating technique, Fig. 11 shows the evolution of the locus of  $Z_1 - Z_2$  events, with various source velocity gates, for the reaction 50 MeV/A  $^{197}\text{Au} + ^{27}\text{Al}$ . The locus of fragment charges for all 2-fold events is shown in the lower left frame, and the gates used for  $V_{source}$  are shown in the upper left frame. The excitation energy inferred from the average linear momentum transfer in each  $V_{source}$  bin is written in each frame, and ranges up to 900 MeV of excitation.

Several trends are observed with increasing excitation energy (i.e. increasing centrality). First, peripheral reactions tend to lead to symmetric fission of the gold-like system. These events are characterized by a sharp peak at  $Z_1 = Z_2 = \frac{Z_{Au}}{2}$  in the first gated frame, for example. (This is also true for the ungated frame, showing the dominance of the peripheral events in the 2-fold coincidence data.) This peak broadens significantly, indicating the onset of asymmetric fission, with increasing centrality of the collision. The peak broadens primarily along a locus of  $(Z_1 + Z_2) \approx Z_{Au}$ , showing that these events are not multibody decays, but rather true binary decays with an increasingly asymmetric nature. Second, the locus of events broadens somewhat towards lower values of fragment charge, and also shifts in absolute scale towards lower values of  $Z$ . This is the typical result expected for light particle evaporation from a hot fissioning system. As the excitation energy increases, the number of light charged particles evaporated will increase, both from the composite system prior to scission, and from the heavy fragments after scission. This broadens and lowers the average values of fragment charge detected with increasing excitation energy, and can be reproduced qualitatively by statistical model calculation of sequential decay [19].

In Fig. 12, a similar result is observed for the reaction 50 MeV/A  $^{197}\text{Au} + ^{nat}\text{Cu}$ . Unlike the Al target, however, more central Cu reactions rapidly lead to very asymmetric binary decays, and then they progress to multibody decays, which contribute a peak at low  $(Z_1 + Z_2)$  values in these 2-fold event plots. The data certainly show a broadening and shifting to lower average charge values, but it seems more extensive, and happens at lower excitation energy for the heavier target. This could be due to the increased angular momentum expected in the heavier composite system. Note also that there exists significantly more Cu events with a very low  $V_{source}$ , that tend to correspond to higher-order decays, with many light fragments. Obviously, the source velocity gating can be performed on the higher order events, with equally interesting results.

### 3.5 Dalitz Plots

To utilize the source velocity gating technique with multibody events, a practical way of representing the data must be chosen. For simple multifragment decays, the 3-fold events,



50 MeV/A  $^{197}\text{Au} + ^{27}\text{Al}$

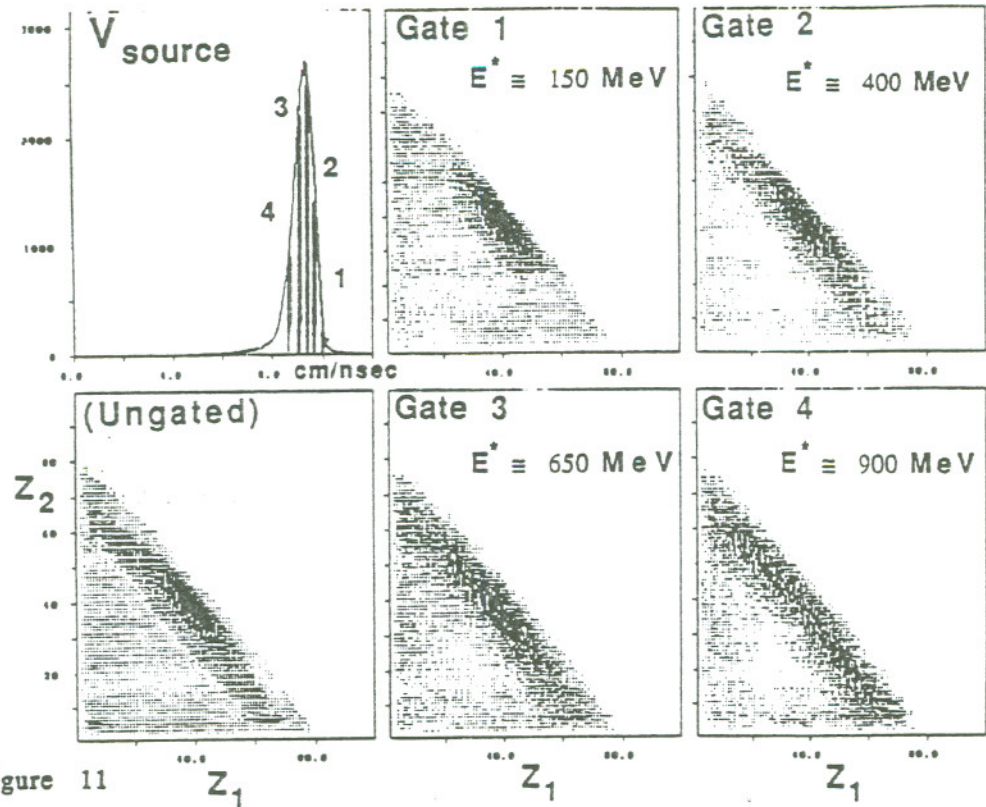


Figure 11

50 MeV/A  $^{197}\text{Au} + \text{natCu}$

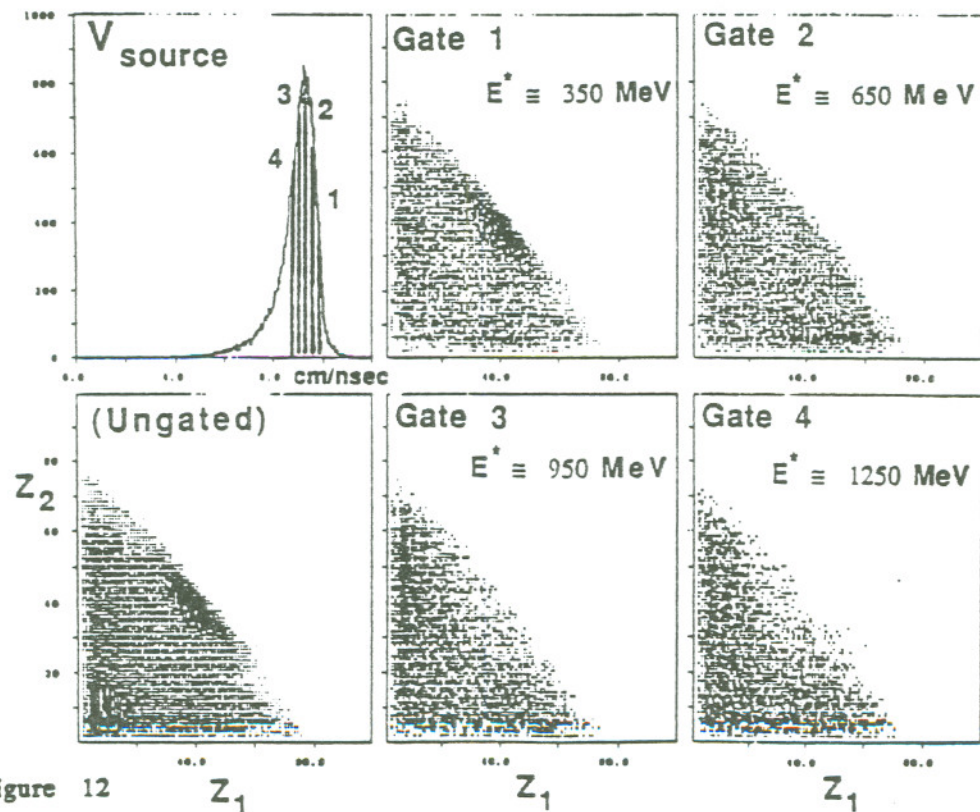


Figure 12

we have elected to use a trigonal axis representation developed long ago for particle physics, known as the Dalitz plot. In Fig. 13, the evolution of Dalitz plots with different source velocity requirements is shown for the 50 MeV/A Au + Al reaction. In all of these plots, the charge of each fragment for a 3-fold event is represented by a unique location on the trigonal axes. The axes are not shown, but they extend from the center of each plot to the top, and from the center to the lower left and right corner of each plot. Each axis plots the value of either  $\frac{Z_1}{Z_{total}}$  or  $\frac{Z_2}{Z_{total}}$  or  $\frac{Z_3}{Z_{total}}$ . In the Dalitz representation, three equally sized fragments would be plotted as a point in the middle, while one large fragment and two light fragments would be plotted towards the end of one axis. Two heavy fragments and one light fragment would be plotted midway between two axes, away from the origin. Thus, the Dalitz representation allows the qualitative distinctions in the three-body decay mass asymmetries to be readily apparent. In the Dalitz plots shown here, the three axes have been symmetrized by randomly assigning  $Z_1$ ,  $Z_2$ , and  $Z_3$ .

In Fig. 13, it is obvious that the more peripheral Au + Al reactions lead to a predominant peak of events where one fragment is relatively light, and the other two fragments are equally sized and heavier. For more central collisions, there is a clear progression towards one heavier fragment, and two equally sized lighter fragments. For the aluminum reactions, there is always a minimum for three equally sized fragments, which is energetically the hardest possibility to form in a sequential decay scheme. In each of these plots, a requirement was placed on the total detected charge of the event ( $Z_{total} < 55$ ), such that the plots are not contaminated by light-fragment coincidences where most of the mass of the event is undetected.

Although the trends observed in these Dalitz plots suggest fragmentation behavior from an excited composite system, that progresses according to the centrality of the reaction, the most useful aspect of these data come from their comparison to simulation. The charge distribution of fragments emitted from sequential binary decays of highly excited composite systems has been simulated by the Monte Carlo code GEMINI[10]. In these simulations, a composite system was chosen that corresponds to the most likely fractional momentum transfer to the gold projectile, observed for the three different source velocities. The results of the simulations are plotted in Fig. 14, together with the experimental data from the same source velocities, on three different targets. There is surprisingly good agreement for all targets for excitation energies below approximately 700 MeV. At higher excitation energies, seen for the copper target in Fig. 14, there is a significant production of 3-fold events that arise from other processes, processes that do not arise from the statistical decay of an equilibrated hot source. Efforts will be made to reconstruct the charge, energy and angular distributions of these other fragments, once the statistical component has been properly subtracted. Refinements in the model for angular momentum transfer in incomplete momentum transfer reactions are needed to make a better approximation of the truly statistical decay component of these spectra.

### 3.6 Correlation Function Analysis

There is another analysis technique that has recently been used to define the timescales of the nuclear fragmentation process[4, 8]. There are predicted to be observable differences between prompt and sequential multifragmentation, measured in the relative velocities and angles of the fragments detected in multibody decays of hot systems. For a truly



50 MeV/A  $^{197}\text{Au} + ^{27}\text{Al}$

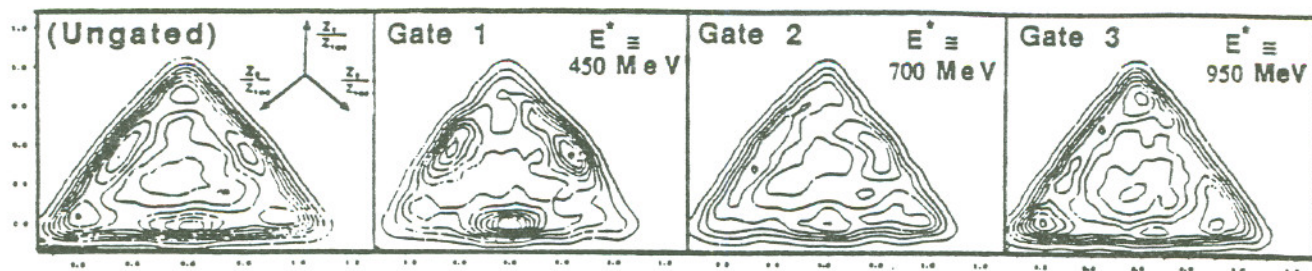


Figure 13

50 MeV/A  $^{197}\text{Au} + ^{12}\text{C}, ^{27}\text{Al}, ^{\text{nat}}\text{Cu}$

Experiment

Simulation

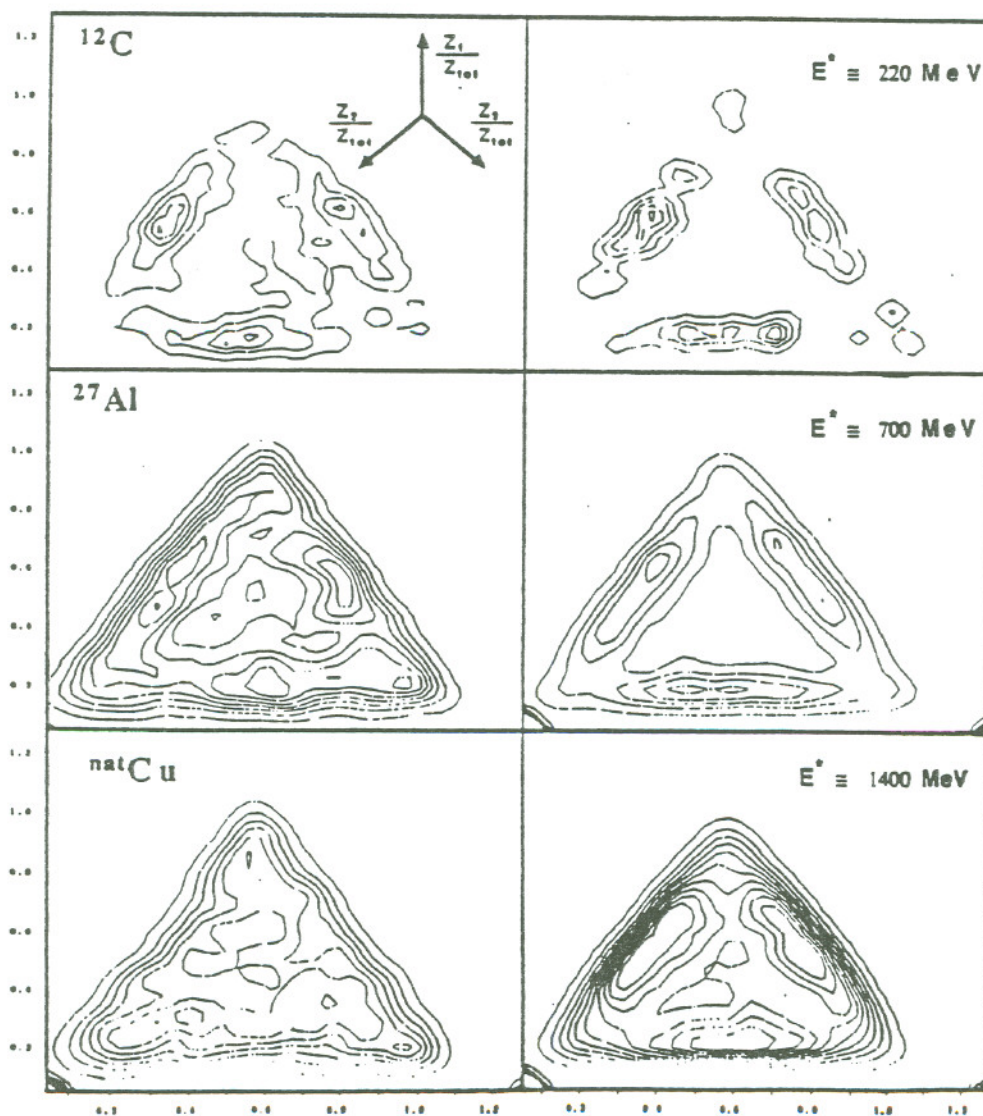


Figure 14

“prompt” multibody decay of a composite system, one would expect that the Coulomb forces of the newly formed fragments force them to break apart with similar relative angles and velocities. For truly sequential statistical decay, on the other hand, one binary scission defines two directions, and a subsequent scission necessarily will have a vectorial sum the velocities of the primary decay and the secondary decay. In a three-body decay, this is often pictured as one fragment going one way, and two fragments going approximately  $180^\circ$  in the other direction. In this simplified picture, there is a very strong correlation in relative velocities and angles for two of the three emitted fragments. Of course, this analysis can be performed for any multibody decay, but we have chosen to begin with the 3-fold events, because Coulomb trajectory calculations have already been performed for a similar system for three-body decays[4].

In Fig. 15, the experimental relative angles and velocities for 50 MeV/A  $^{197}\text{Au} + ^{27}\text{Al}$  is shown, together with the simulations developed for 60 MeV/A  $^{22}\text{Ne} + ^{197}\text{Au}$ [4]. A correlation function was constructed for the relative velocities ( $R(V_{rel})$ ) and relative angles ( $R(\theta_{rel})$ ) of each of the three pairs of fragments in a triple event. A correlation function is simply the measured values of the real events divided by the values obtained from uncorrelated or random events. If there is a real correlation in the data, then dividing by the correlations obtained from constructed “fake” events will highlight the differences without the usual geometric efficiency biases brought about in simulations. For these data in particular, each “fake” event was constructed from choosing one fragment from each of three different 3-fold events. Thus, all the data is real, and suffers the same kinematic bias, but the “fake” events cannot be physically correlated in space and time. The correlation function is then constructed by the following formula:

$$R(x) = \frac{(Y_p - Y_u)}{(Y_p + Y_u)} \quad -1 < R < +1 \quad (2)$$

where  $x$  is either  $V_{rel}$  or  $\theta_{rel}$ , and  $Y_p$  and  $Y_u$  are the values of the physical and uncorrelated events, respectively. The quantities  $Y_p$  and  $Y_u$  are constructed from the same number of events to normalize the magnitude of the correlation function between -1 and 1. The data shown in Fig. 15 have the arbitrary designation where 1 is the lightest fragment, 3 is the heaviest, and 2 is the intermediate fragment.

In Fig. 15, it is immediately obvious that real correlations do exist in the data, the most obvious one being the dip at low values of  $V_{rel}$  and  $\theta_{rel}$  caused by Coulomb repulsion between the fragments. The heavier the fragments are, the larger the low relative velocity dip becomes. The prompt multifragmentation simulations (depicted by the dotted lines) are based simply on Coulomb trajectory calculations of three fragments, initially in contact with each other. They show more or less equal velocity and angular separation for every pair of fragments. The sequential decay calculations (plotted as the solid lines) demonstrate that in sequential decay, two fragments can be emitted at low relative velocity and angle, although that may not be the most probable decay mode. The data show clear agreement with the sequential calculations, although the comparison with the sequential decay simulations that include a final state interaction (shown as the dash-dot lines) does show the best agreement. This simulation is reported to be for sequential decay on a short timescale ( $\tau = 300 \text{ fm/c}$ ), where the emitted fragments still exert a final state interaction on each other.

This type of data analysis is also amenable to the source velocity conditions demon-



50 MeV/A  $^{197}\text{Au} + ^{27}\text{Al}$

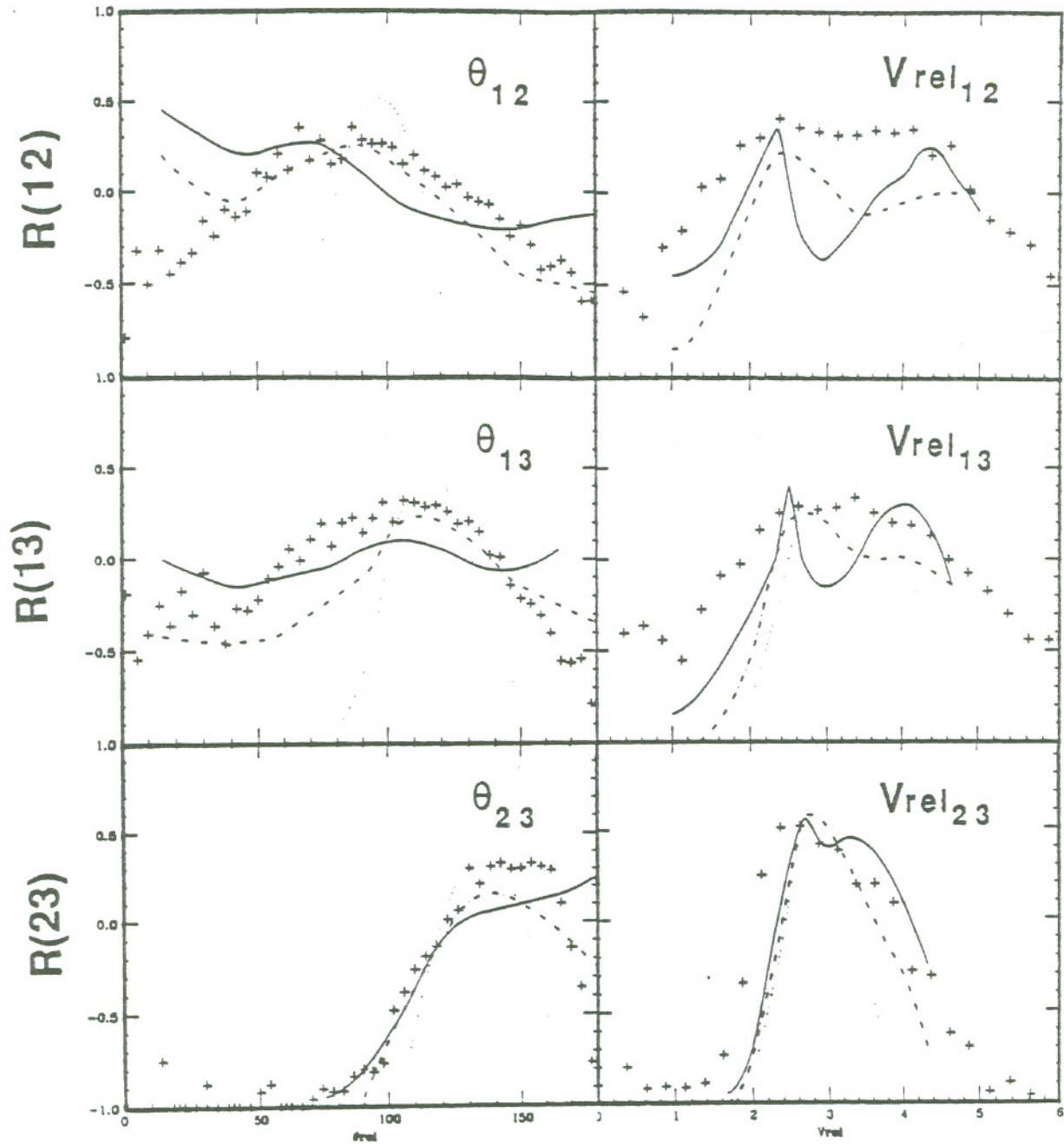


Figure 15

strated earlier, and can also be done for all three targets for all multifold events. Preliminary results of the source velocity analysis of the correlation functions shows promise, and will be developed fully in the coming months.

#### ACKNOWLEDGEMENTS

This work was supported by the Director, Office of Energy Research, Division of Nuclear Physics of the Office of High Energy and Nuclear Physics of the US Department of Energy under contract DE-AC03-76SF00098. The following people performed this experiment: D. R. Bowman, N. Colonna, D. N. Delis, K. Hanold, K. Jing, M. A. McMahan, L. G. Moretto, G. J. Wozniak, S. Angius, I. Iori, A. Moroni, G. Guarino, and A. Pantaleo, W. L. Kehoe, B. Libby and A. C. Mignerey.

#### References

- [1] G. J. Wozniak, N. Colonna, R. J. Charity, and L. G. Moretto, *Proceedings, XII Nuclear Physics Symposium, Oaxtepec*, World Scientific (1989).
- [2] D. R. Bowman, G. F. Peaslee, N. Colonna, M. A. McMahan, H. Han, K. Jing, D. Delis, G. J. Wozniak, L. G. Moretto, W. L. Kehoe, B. Libby, A. Marchetti, A. C. Mignerey, A. Moroni, S. Angius, A. Pantaleo, and G. Guarino, *Proceedings, XXVII International Winter Meeting on Nuclear Physics*, Bormio, Italy, (1989).
- [3] L. G. Moretto, And G. J. Wozniak *Prog. Part. Nuc. Phys.* 21, 401, (1988).
- [4] R. Bougault, J. Colin, F. Delaunay, A. Genoux-Lubain, A. Haifani, C. LeBrun, J. F. Lecoilley, M. Louvel, and J. C. Steckmeyer, *Phys. Lett. B*232, 291 (1989).
- [5] D. Pelte, U. Winkler, M. Gnirs, A. Gobbi, K. D. Hildenbrand, R. Novotny, *Phys. Rev C*39, 553 (1989).
- [6] D. H. E. Gross, G. Klotz-Engmann, and H. Oeschler, *Phys. Lett. B*224, 29 (1989).
- [7] J. Pochodzalla, W. Trautmann, and U. Lynen, *GSI Preprint* (1989).
- [8] R. Trockel, U. Lynen, J. Pochodzalla, W. Trautmann, N. Brummund, E. Eckert, R. Glasow, K. D. Hildenbrand, K. H. Kampert, W. F. J. Müller, D. Pelte, H. J. Rabe, H. Sann, R. Santo, H. Stelzer, and R. Wada *Phys. Rev. Lett.*, 59, 2844 (1987).
- [9] R. J. Charity, D. R. Bowman, Z. H. Liu, R. J. McDonald, M. A. McMahan, G. J. Wozniak, L. G. Moretto, S. Bradley, W. Kehoe, and A. C. Mignerey, *Nuc. Phys. A*476, 526 (1988).
- [10] R. J. Charity, M. A. McMahan, G. J. Wozniak, R. J. McDonald, L. G. Moretto, D. G. Sarantities, L. G. Sobotka, G. Guarino, A. Pantaleo, L. Fiore, A. Gobbi, and K. D. Hildebrand, *Nuc. Phys. A*483, 371 (1988).
- [11] R. J. Charity, K. X. Jing, D. R. Bowman, M. A. McMahan, G. J. Wozniak, L. G. Moretto, N. Colonna, G. Guarino, A. Pantaleo, L. Fiore, A. Gobbi, and K. D. Hildebrand, *submitted to Nuc. Phys.* LBL-26859.



- [12] J. T. Walton, H. A. Sommer, G. J. Wozniak, G. F. Peaslee, D. R. Bowman, W. L. Kehoe, and A. Moroni, *IEEE Trans. Nuc. Sci.* , (in press 1989).
- [13] W. L. Kehoe *PhD Thesis*, Chemistry Dept., Univ. Maryland, College Park (1989).
- [14] J. B. Moulton, J. E. Stephenson, R. P. Schmitt, and G. J. Wozniak, *Nuc. Instr. and Meth.* 157, 325 (1978).
- [15] G. F. Peaslee, *Unpublished data* (1990).
- [16] V. E. Viola, *Nuc. Phys.* A471, 53 (1987).
- [17] D. Guerreau in *International School on Nuclear Physics: Nuclear Matter and Heavy Ion Collisions*, Les Houches, France (Feb, 1989), Preprint GANIL P89-07 and references therein.
- [18] N. Colonna, R. J. Charity, D. R. Bowman, M. A. McMahan, G. J. Wozniak, L. G. Moretto, Guarino, A. Pantaleo, L. Fiore, A. Gobbi, and K. D. Hildenbrand, *Phys. Rev. Lett.* 62, 1833 (1989).
- [19] G. F. Peaslee, R. Regimbart, G. J. Wozniak, and L. G. Moretto, *Presented at Am. Phys. Soc. Meeting*, Santa Fe, (1988).
- [20] Y. Blumenfeld, N. Colonna, D. N. Delis, K. Hanold, J. C. Meng, G. F. Peaslee, G. J. Wozniak, L. G. Moretto, B. Libby, G. Guarino, N. Santoruvo, and I. Iori *submitted to Phys. Rev. Lett.*, (1990).

### Figure Captions

1. Schematic velocity diagram of "reverse kinematics", where a large projectile is incident on a small target nucleus. There is a large center-of-mass velocity ( $V_{cm}$ ) and a relatively small fragment emission velocity ( $V_e$ ) from the composite system. All fragments emitted into the cross-hatched area will be detected by the detector shown.
2. Photograph of one expanded telescope of the Si-Si-Pl array. (See text).
3. Photograph of the Si-Si-Pl array as it was configured for the 50 MeV/A  $^{197}\text{Au}$  beam. The beam is incident on a target off to the left, and then passes through the central hole in each array. The upstream array is 37 cm from the target, and the downstream array is 103 cm from the target.
4. Typical charge (left frame) and position (right frame) resolution obtained in one telescope of the Si-Si-Pl array.
5. Contours of the experimental cross section  $d^2\sigma / dV_{||}dV_{\perp}$  in the  $V_{||} - V_{\perp}$  plane, for typical fragments of charge Z detected in the reaction 50 MeV/A  $^{197}\text{Au} + ^{12}\text{C}$ .

6. Contours of the experimental cross section  $d^2\sigma / dV_{||}dV_{\perp}$  in the  $V_{||} - V_{\perp}$  plane, for fragments of charge  $Z=20$ , detected in the reactions 50 MeV/A  $^{197}\text{Au} + ^{12}\text{C}$ ,  $^{27}\text{Al}$ , and  $^{nat}\text{Cu}$ .
7. Integrated singles cross sections for the reactions 50 MeV/A  $^{197}\text{Au} + ^{12}\text{C}$ ,  $^{27}\text{Al}$ , and  $^{nat}\text{Cu}$ .
8. Fragment charge  $Z_1$  versus fragment charge  $Z_2$ , for binary events (left side) and triple events (right side) in the reactions 50 MeV/A  $^{197}\text{Au} + ^{12}\text{C}$ ,  $^{27}\text{Al}$ , and  $^{nat}\text{Cu}$ . For triple events, the charge of two randomly selected fragments is plotted against the third. A dashed line is drawn on the line  $Z_1 + Z_2 = Z_{proj}$ .
9. The total detected charge plotted against the excitation energy inferred from the source velocity, for the reactions 50 MeV/A  $^{197}\text{Au} + ^{12}\text{C}$ ,  $^{27}\text{Al}$ , and  $^{nat}\text{Cu}$ .
10. The total number of multibody events, expressed as a fraction of 1 (where 1 equals all multibody events) plotted against the excitation energy per nucleon inferred from the source velocity, for the reactions 50 MeV/A  $^{197}\text{Au} + ^{12}\text{C}$ ,  $^{27}\text{Al}$ , and  $^{nat}\text{Cu}$ .
11. The  $Z_1$  versus  $Z_2$  plots for the reaction 50 MeV/A  $^{197}\text{Au} + ^{27}\text{Al}$ , ungated and gated by different source velocities. The source velocity distribution and the four gates are shown in the upper left plot, where the decreasing source velocity leads to an increased inferred excitation energy, shown in each frame.
12. Same as Fig. 11 for the reaction 50 MeV/A  $^{197}\text{Au} + ^{nat}\text{Cu}$ .
13. Gated and ungated Dalitz plots for the reaction 50 MeV/A  $^{197}\text{Au} + ^{27}\text{Al}$ . Each of the three trigonal axes corresponds the value of  $Z_1/Z_{total}$ ,  $Z_2/Z_{total}$ , or  $Z_3/Z_{total}$ . The righthand plots have been gated by source velocity.
14. Gated Dalitz plots for the reactions 50 MeV/A  $^{197}\text{Au} + ^{12}\text{C}$ ,  $^{27}\text{Al}$ , and  $^{nat}\text{Cu}$  (left column), compared to GEMINI results for comparable systems (right column). The excitation energies used in the simulations have been matched to the source velocity gates on the data.
15. Relative velocity (left column) and relative angle (right column) correlation functions for the reaction 50 MeV/A  $^{197}\text{Au} + ^{27}\text{Al}$  (data shown as crosses). Overlaid are three simulations run for the 60 MeV/A  $^{22}\text{Ne} + ^{197}\text{Au}$  system[4]. The dotted line corresponds to true "prompt" multifragmentation, the solid line corresponds to a true sequential statistical calculation, and the dot-dashed line corresponds to a sequential decay that includes some final-state interaction terms.